Journal of Physics and Chemistry of Solids xxx (xxxx) xxx

Contents lists available at ScienceDirect

Journal of Physics and Chemistry of Solids

journal homepage: www.elsevier.com/locate/jpcs

Strontium stannate as an alternative anode for Na- and K-Ion batteries: A theoretical study

Yohandys A. Zulueta [a], Minh Tho Nguyen [b,c], My-Phuong Pham-Ho [d,e,*]

[a] Departamento de Física, Facultad de Ciencias Naturales y Exactas, Universidad de Oriente, CP- 90500, Santiago de Cuba, Cuba
[b] Institute for Computational Science and Technology (ICST), Ho Chi Minh City, 700000, Viet Nam
[c] Department of Chemistry, KU Leuven, Celestijnenlaan 200F, B-3001, Leuven, Belgium
[d] Faculty of Chemical Engineering, Ho Chi Minh City University of Technology (HCMUT), 268 Ly Thuong Kiet Street, District 10, Ho Chi Minh City, Viet Nam
[e] Vietnam National University Ho Chi Minh City (VNU-HCM), Linh Trung Ward, Thu Duc District, Ho Chi Minh City, Viet Nam

ARTICLE INFO

Keywords:
Anode
Strontium stannate
Alkali-ion battery
Defect energetics
Alkali ion transport properties
Alkali ion migration mechanism

ABSTRACT

Theoretical predictions on structural, electronic and transport properties of pristine and alkali-doped strontium stannate ($SrSnO_3$) were made using density functional theory and force field methods. Results of electronic structure computations show that a doping of alkali-ion (Li^+, Na^+ and K^+) into $SrSnO_3$ induces the apparition of extra energy bands on the valence and conduction bands and small translation of the valence and conduction band limits. This is more accentuated in K^+-ion doped samples with lower energy gap. Defect energetics computations reveal a low energetic cost associated the alkali incorporation mechanism proposed in this work. Such a mechanism provides us with an intermediate first discharge reaction to describe the delithiation process. Results on alkali ion transport properties in interstitially doped nanocrystalline $SrSnO_3$ samples reveal lower diffusion activation energies of 0.25, 0.28 and 0.44 eV and diffusion coefficient at 25 °C of 9.6, 2.9×10^{-11} and 4.8×10^{-13} cm^2s^{-1} for Li-, Na- and K-doped samples, respectively. These predicted properties bring in new evidence to stimulate a consideration of strontium stannate for use as an alternative anode, in particular for both Na- and K-ion batteries.

1. Introduction

The alkaline earth (A^+) stannates $MSnO_3$ (M = Sr, Ca, Ba) have extensively been studied [1–14] in part due to their important industrial application features for, among others, the dielectricity, photocatalyst, superconductivity, photoelectric sensors, capacitor components, solid oxide fuel and li-ion batteries (LIB). Especially, the strontium stannate $SrSnO_3$ (SSO) based materials are involved in other related applications such as transparent solar photovoltaics and displays [10,11]. The distorted perovskite SSO exhibits an orthorhombic structure (space group Pbnm) at ambient temperature and is based on tilted octahedra. It takes four phase transitions upon heating going from a space group of Pbnm to a Pm3 m when octahedral tilts are removed [12,13].

Numerous synthetic methods have been proposed leading to SSO based materials with improved physicochemical properties [1–9]. On the other hand, doping has been known as one of the effective ways of improving the properties of a material. For instance, upon doping with La at the Sr-site, the transparent conducting properties of SSO are enhanced thanks to an avoidance of SnO_6 octahedral tilting [12]. The shape and size of SSO materials, such as monocrystal, polycrystal, powder, nanoparticles and nanorods, are also key factors for improvement of their physicochemical properties. Chao et al. [7] reported that the use of $SrSn(OH)_6$ as the main precursor for their synthesis of SSO nanorods. These authors proposed a possible formation mechanism of SSO with a nanorod structure under certain conditions for a promising electrochemical performance in LIBs. In addition, Hu et al. [8] reported that a calcination of the hydrothermally synthesized $SrSn(OH)_6$ nanowires could also produce SSO nanorods. It is worth noting that the SSO nanorods show a longer cyclability with a capacity of 200 mAh/g (over 50 cycles) than that of SSO nanoparticles [8].

There are in general various key requirements for a material to be used as an electrode in alkali-ion batteries [13]. Indeed, for providing a good cyclability the material should a) well react reversibly with the alkali-ion, b) possess a good electronic and ionic conducting, and c)

* Corresponding author. Faculty of Chemical Engineering, Ho Chi Minh City University of Technology (HCMUT), 268 Ly Thuong Kiet Street, District 10, Ho Chi Minh City, Viet Nam.
E-mail address: phmphuong@hcmut.edu.vn (M.-P. Pham-Ho).

https://doi.org/10.1016/j.jpcs.2021.110505
Received 8 September 2021; Received in revised form 4 November 2021; Accepted 21 November 2021
Available online 24 November 2021

rapidly behave on insertion and removal of alkali-ion by accepting at least one alkali-ion per unit cell to ensure a high capacity, power density, and fast alkali-ion diffusion [13]. Based on these requirements, the SSO have been considered as an anode in LIBs [7,8]. However, none of previous studies have explored the full discharge process and particularly Li-diffusion mechanisms.

As far as the theorical approaches on these systems are concerned, atomic simulations are well recognized as a valuable technique for prediction of physicochemical properties of compounds and other processes, for example defect chemistry, diffusion and mechanical stability [15–26]. Density functional theory (DFT) is effective for investigation of the underlying conditions of small structures [15–17,21–26]. While large scale molecular dynamics (MD) simulations are ideal for reproducing and/or predicting the transport properties in nanostructures, force field-based simulations are convenient for an analysis of defect energetics [16–21].

In our recent work [27] the intrinsic Li-insertion mechanism was revealed, including the performance of SSO as an anode in LIB. Structural, electronic, mechanical and transport properties of SSO were determined using both DFT computations and force-field-based simulations [27]. Accordingly, SSO is calculated to exhibit an indirect energy gap of ~3.0 eV, in agreement with experiment [23–27]. SSO is mechanically stable and more isotropic with respect to the volume change than the shape change. A comparison of the Li-ion transport properties of Li-doped mono- and nanocrystalline SSO samples emphasizes that the nanocrystalline material is characterized by a lower diffusion activation energy and a higher diffusivity at the operative temperature [27].

To the best of our knowledge, there is no report yet concerning the Na- and K-transport properties and their migration mechanism in SSO. Strontium stannate has interstitial sites where other alkali metal ions such as Na^+ and K^+ can be accommodated, suggesting the need of similar studies to explore the capability of SSO as an anode in Na- and K-Ion batteries.

Despite the current progress in Na- and K-ion batteries development, the search of efficient anodes is still a candent research topic [28–33]. In this context, we set out to perform a theoretical study with the aim to determine the electronic and transport properties of the pristine and alkali-doped $SrSnO_3$ (A-SSO) using DFT and force field-based methods. In this paper we propose an interstitial incorporation mechanism for the alkali-ion A^+ ($A^+ = Li^+$, Na^+ and K^+) into the SSO lattice structure, giving a reasonable understanding of the alkali insertion/de-insertion process as well as the large-scale diffusion mechanism in A-SSO nanocrystalline sample. Study of alkali transport properties in SSO structure would drive further exploration and experiment on the actual capability of this material for Na- and K-ion battery applications.

2. Methodology

Fig. 1a displays the unit cell of $SrSnO_3$ in the conventional representation. The orthorhombic SSO is characterized as a distorted perovskite type structure with a [SnO_2] tilted octahedral having the lattice parameters a = 5.697 Å, b = 8.052 Å and c = 5.699 Å. The CASTEP computer code [34] is used to probe the influence of the inclusion of Li^+-, Na^+- and K^+- ion onto the electronic structure of SSO. The cell parameters and atomic positions of pristine SSO are adopted from our previous work [27] to study the A-SSO, where the RPBE exchange-correlation functional is employed within the generalized gradient approximation (GGA) [34–36]. The pseudo atomic functionals for Li-$2s^1$, Na-$3s^1$, K-$4s^1$, O-$2s^2$ $2p^4$, Sr-$4s^2$ $4p^6$ $5s^2$ and Sn-$5s^2$ $5p^2$ in the reciprocal representations are used. The net charge of system of +1 (formal charge of the A^+-ion) for A-SSO is adopted during the band structure and density of the state computations. In this case, alkali ions are interstitially located as shown in Fig. 1b. The plane-wave energy cut-off of 600 eV is adopted for the standard norm-conserving pseudopotentials. The convergence thresholds criteria are taken with a total energy per atomic convergence tolerance of 1×10^{-5} eV, resulting in an eigen-energy convergence tolerance of 2.73 eV. A custom *k*-point set of 4 × 3 × 4 for SSO (space group P1) is used to calculate the total and projected density of states in the SSO conventional representation. A Γ-centered Monkhorst-Pack scheme is used to sample the Brillouin zone [37].

The General Utility Lattice Program (GULP) is used to perform lattice static calculations.[38] The force-field parameters used in this work contain two main components, namely, Buckingham-type potentials that are used to model the short-range interactions, and Coulombic forces for long-range interactions. These parameters are taken from the literature and our recent works [18,19,27]. To complete the force-field parametrization, the shell model [39] is included for static simulations to consider ion polarization for the O–O interactions. The Broyden–Fletcher–Goldfarb–Shanno (BFGS) method [38] is used to update the cell parameters and fractional positions of the equilibrium SSO lattice structure.

The LAMMPS code [40] is used to determine the alkali diffusion via force-field based MD simulations. In this study the transport properties of nanocrystalline A-SSO samples are predicted. To build the nanocrystals, we first set simulation boxes of 5 × 3 × 5 supercells of SSO, with 1650 ions (150 A^+, 300 Sn^{4+}, 300 Sr^{2+}, and 900 O^{2-}) with periodic boundary conditions. These initial supercells are taken as a random seed to generate polycrystals of 80 × 80 × 80 $Å^3$ (3728-A^+, 7478 Sn^{4+}, 5621 Sr^{2+} and 22441 O^{2-} ions, leading a similar A^+ concentration) with 12 grains employing the Voronoi tessellation method using the Atomsk code [41] (see Fig. 1c). Due to the tessellation process and the introduction of the A^+ ions, additional charge in the simulation boxes is expected, which is balanced introducing Sr vacancies randomly.

The first step involves the use of an isothermal-isobaric ensemble (NTP) to equilibrate the simulation boxes. After equilibration, the NVT ensemble is used to produce, record, and calculate the mean square displacement (MSD) of the A^+ ions to obtain the diffusion coefficient (D)

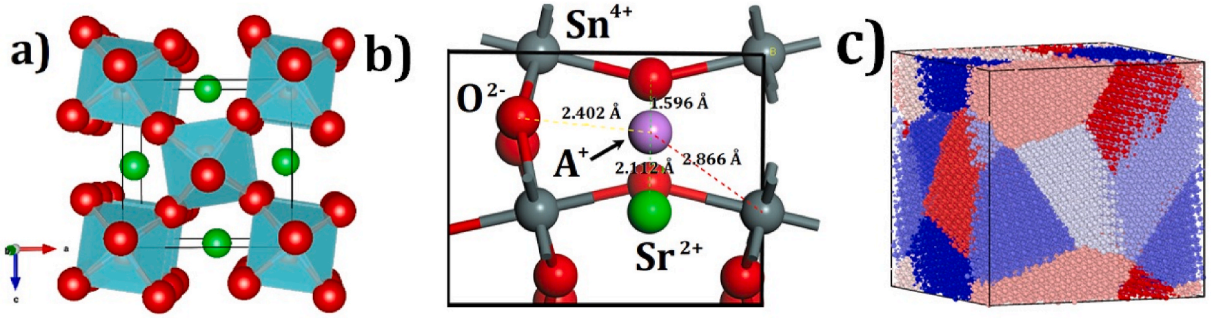

Fig. 1. a) Crystal structure of $SrSnO_3$, **b)** alkali interstitial site in $SrSnO_3$ where the alkali-nearest neighbor distances are included. Green, red and blue balls represent the Sr^{2+}, O^{2-} and A^+ ions, cyan polyhedron in a) represents the [SnO2] octahedral, and **c)** polycrystalline (with 12 grains) of $SrSnO_3$ sample, color coding is referred to a unique grain.

from the slope of the straight-line MSD vs time plots:

$$\mathrm{MSD} = 6\mathrm{D}t \quad (1)$$

where t is the simulation time. For MD simulations the production run is limited to 2 ns with a time step of 2 fs and the temperature ranges between 800 and 1200 K. Alkali migration is a thermally activated process quantified by an Arrhenius-type dependence between diffusion coefficient and the temperature. In this sense the activation energy for diffusion is obtained by equation (2):

$$D = D_0 exp(-E_a / K_B \mathrm{T}) \quad (2)$$

where D_0 is the diffusion coefficient at high temperature, E_a the diffusion activation energy, K_B the Boltzmann constant and T the temperature [16,17].

3. Results and discussion

3.1. Effect of the alkali introduction on the electronic structure of $SrSnO_3$

Electronic properties are imperatively needed for evaluation of the performance of energy storage devices. Compounds considered for energy storage applications must indeed be efficient electronic and ionic conductors [13]. Electronic properties are examined with the aim of revealing the effect of the alkali inclusion on the electronic structure of SSO. Fig. 2 displays the calculated total (DOS) and partial (PDOS) density of states of Li^+-, Na^+- and K^+-doped SSOs. As it was described in our previous work on pristine case [27] the energy gap value of SSO depends on the relative energy position of O-2*p* and Sn-5*p* states. While the PDOSs at the conduction band are dominated by the Sn-5*p* states, while the valence band by the O-2*p* states. The O-2*p* states have a small contribution to the conduction band, and the Sn-5*p* atomic orbitals have small role on the electronic properties in the valence band. The overlap of Sn-5*p* and O-2*p* levels at the valence and conduction bands is an

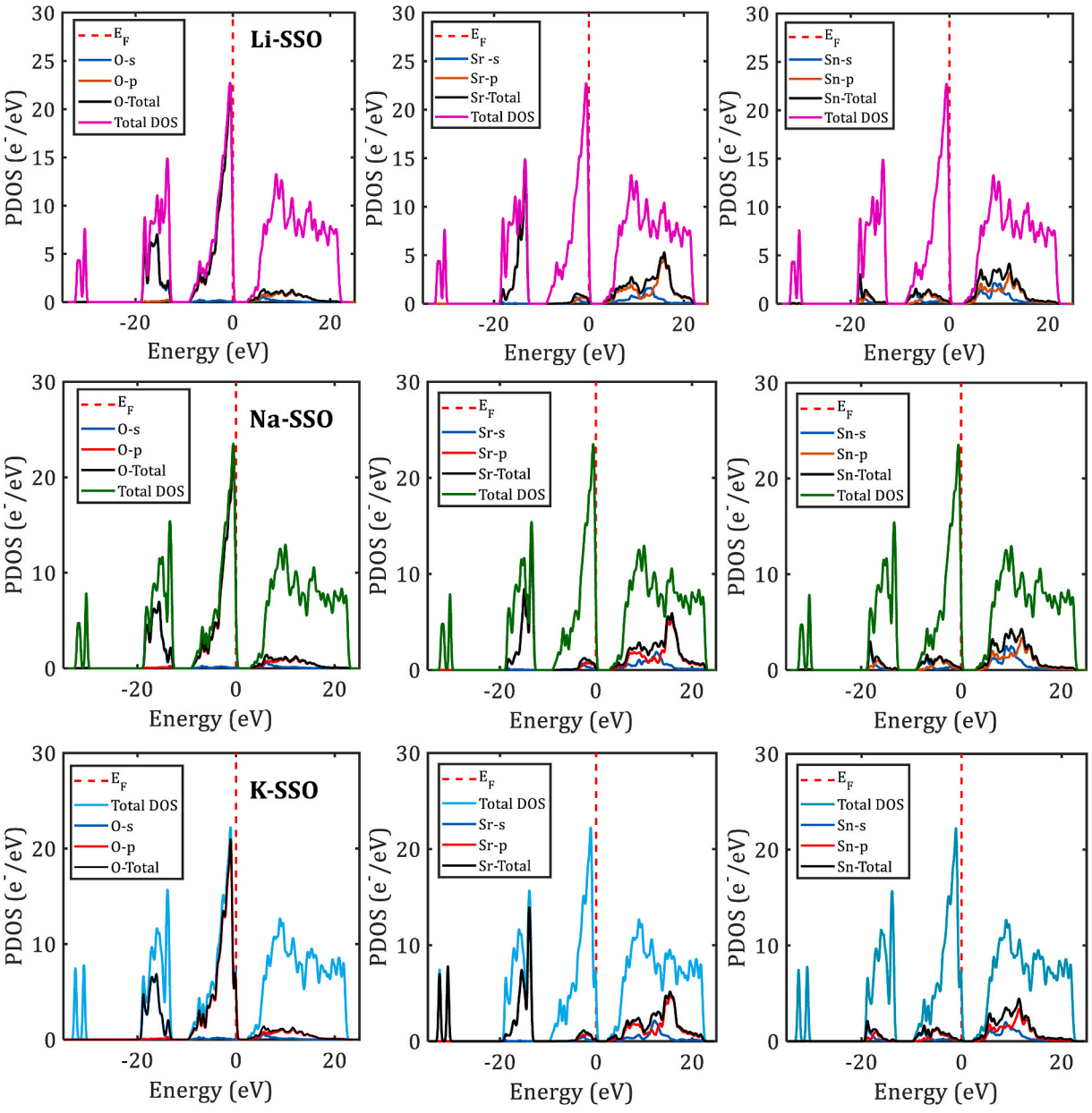

Fig. 2. Densities of the states (DOS) and projected densities of the states (PDOS) of A^+-doped $SrSnO_3$. SSO denotes $SrSnO_3$ and A-SSO is referred to A^+-doped $SrSnO_3$.

indicator of a bonding−antibonding energy splitting for Sn-5*p* and O-2*p* hybrid states, resulting in a SnO_6 octahedral hybridization.

In order to investigate the effect of an A^+-ion inclusion, PDOS of each host species of A-SSO structures are depicted in Fig. 3 a, b and c. As it is shown, addition of A^+-ions induces the apparition of extra energy bands on the valence and conduction bands and small shift of the valence and conduction band limits.

Fig. 3d depicts the PDOS of Li^+-, Na^+- and K^+-ions. For the three cases considered, a larger contribution is noticeably made to the conduction band; therefore Na-3*s* orbitals appear to contribute more at higher energy level to the conduction and valence bands. At the conduction band, the PDOS curve of K-4*s* is clearly sharper (i.e. more peaks) than for those of Na-3*s* and Li-2*s*, which implies that, as a consequence, larger contributions to the levels of the conduction band spectra tend to reduce the Eg.

The computed values of Eg are ~3.0 eV for both Li- and Na-SSO, whereas it amounts to 2.3 eV for K-SSO. These Eg values for Li- and Na-SSO are in line with the predicted values for pristine SSO and experiment [27]. The inclusion of large K^+-ion into the SSO lattice structure modifies the electronic structure of SSO by a reduction of the Eg values. In summary, a doping of alkali metal ions in SSO results in a significant improvement of electronic properties by adding extra energy bands at valence and conduction bands, and reducing the Eg values with direct implication on the electrochemical windows in battery applications.

3.2. Defect chemistry of alkali-doped $SrSnO_3$

In order to identify the alkaline interactions with the SSO lattice structure, defect energetics computations are performed, in considering only the A^+ interstitial and Sr-vacancy as point defects. Description of other types of point defects can be found in Refs. [18,19].

Equation (3) is proposed to describe the A^+ incorporation mechanism into the SSO lattice structure:

$$A_2O + Sr_{Sr} \rightarrow 2A_i^{\bullet} + V_{Sr}'' + SrO \quad (3)$$

where Sr_{Sr}., $A_i^{\bullet}$ and V_{Sr}'' represents strontium ion at its crystallographic site in SSO, A^+ introduced interstitially and strontium vacancy. SrO and A_2O (A^+ = Li^+, Na^+, K^+) denotes strontium and alkaline oxides, respectively. In equation (3), for each two $A_i^{\bullet}$ in the SSO lattice structure one V_{Sr}'' is created in the defective A-SSO to maintain the charge neutrality of the system, leading the stoichiometric formula $A_{2x}Sr_{1-x}SnO_3$.

The solution energy (E_s) is computed by equation (4):

$$E_s = \frac{1}{2}\left(2E_i^A + E_{vac}^{Sr} + E_L^{SrO} - E_L^{A_2O}\right) \quad (4)$$

where E_i^A represents the energy of the inclusion an A^+ ion in an interstitial site, E_{vac}^{Sr} the energy of a Sr-vacancy creation, E_L^{SrO} and $E_L^{A_2O}$ the lattice energies of SrO and A_2O oxides, respectively.

The binding energy (E_B) of $A_i^{\bullet}$ -V_{Sr}'' - $A_i^{\bullet}$ interaction is computed from the calculated defect cluster energy from the trimer and the energies of the isolated V_{Sr}'' and $A_i^{\bullet}$ defects. The final solution energy (E_F) is obtained by the difference between the solution energy and a fraction of the binding energy related to incorporation mechanisms.

The two-region strategy [42] is now used for the calculation of binding and substitution energies. In this method, the crystal structure is divided into two concentrical spherical regions where the radius of the inner sphere is smaller than that of the external region. The isolated defect or defect cluster is placed at the inner sphere with strong interaction between the defect/cluster with the local structure. A quasi–continuum approximation is assumed for the outer region for ionic interactions [42]. Radius values for the inner and outer regions of 13 and 25 Å, respectively, are selected after convergence proofs to obtain the best accuracy. The computational procedure for defect energetics used in this work has previously been applied to describe and evaluate the defect formation and migration in other materials [15,16,18,19]. Computations of solution, binding and final solution energies provide useful information regarding transport properties, bonding nature and more importantly, doping strategies to improve transport properties of ionic compounds [15,16,18,19].

Table 1 summarizes the results of defect energetics computations.

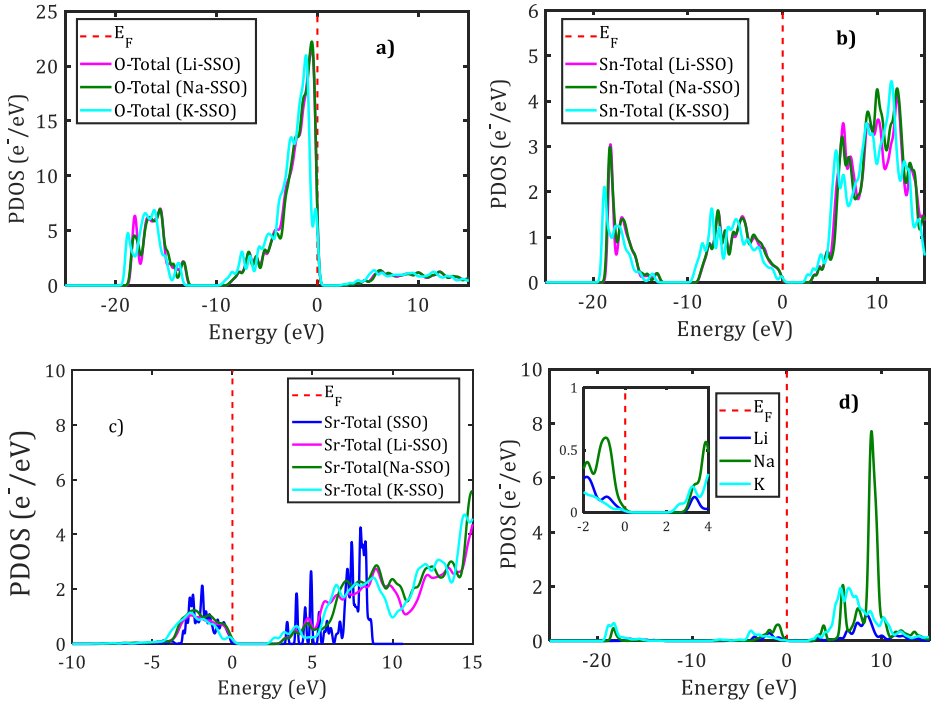

Fig. 3. Total densities of states of a) O^{2-}, b) Sn^{4+} and c) Sr^{2+} of A^+-doped $SrSnO_3$ (A^+ = Li^+, Na^+ and K^+) where SSO denotes $SrSnO_3$ and A-SSO is referred to A^+-doped $SrSnO_3$. d) densities of the states Li^+, Na^+ and K^+, the subfigure inset is an augmented PDOS near the forbidden bands range.

Table 1
Results of defect energetics computations (values for the Li^+ dopant are taken from Ref. [27]).

Alkali ion (Ionic Radius)	E_i^A (eV/defect)	E_{vac}^{Sr} (eV/defect)	E_L^{SrO} (eV/fu)	$E_L^{A_2O}$ (eV/fu)
Li (0.76 Å)	−5.88	19.27	−35.26	−31.32
Na (1.02 Å)	−2.53			−26.93
K (1.38 Å)	0.61			−23.42
Alkali ion (Ionic Radius)	E_s (eV/dopant)	Cluster Energy (eV/defect)	E_B (eV/defect)	E_F (eV/dopant)
Li (0.76 Å)	1.79	4.34	−3.16	0.20
Na (1.02 Å)	2.94	9.13	−5.08	0.40
K (1.38 Å)	4.33	15.74	−4.74	1.95

Upon ionic radius, the SSO accepts inclusion of A^+ interstitially with low values of E_i^A. Results concerning Li^+ ion was already discussed in our previous work [27]. The small (positive) E_i^A value in the case of K^+ ion indicates a structural rejection of the interstitial inclusion of K^+. Negative binding energy of $A_i^\bullet$ -V''_{Sr} - $A_i^\bullet$ cluster provides us with an evidence for the Sr-vacancy trapping effect of A^+-ions. Such an effect is more emphasized for Na^+ dopant with lower binding energy. While the final solution energy for the K^+ dopant is the highest value of 1.95 eV/dopant, those for Na^+ and Li^+ ions amount to 0.40 and 0.20 eV/dopant, respectively. The tendency of E_F value is quite similar to E_s following a change of the A^+ ionic radius. The lower values of E_F for Li^+ and Na^+ emphasize the stronger $A_i^\bullet$ -V''_{Sr} - $A_i^\bullet$ interactions, thus facilitating an $A_i^\bullet$-ion migration at higher temperature. Despite the unfavorable defect energetic results for K^+, the values of solution and binding energies are similar to the reported values for divalent/pentavalent dopants substitution [18,19]. Computed results of defect energetics computations point out that the A^+ incorporation mechanism, described by equation (3), explain satisfactorily the reactivity of the alkali-ion with the SSO host structure, with implications on the performance of SSO as anode [13,27].

3.3. Alkali diffusion in nanocrystalline $SrSnO_3$

Studies concerning the first discharge process in $SrSnO_3$ have been reported [7,8]. Similar to other Sn-containing compounds, it was accepted that an SSO anode is operative in two steps, namely a conversion and an alloying/dealloying process [7,8,43–45]. Other intermediate reactions dealing with Li- and Na-intercalation into an SnO_2 anode have been emphasized by both theoretical computations and scanning transmission electron microscopy measurements [43–46]. Compared to other Sn-containing anodes, the discharge process of SSO is still incomplete due to the lack of a reasonable description of the alkali ion diffusion. To complete the discharge reaction, we can extrapolate the intermediate step from SnO_2 to $SrSnO_3$ anode and would thereby propose a complete set of first discharge reactions as follows:

$$SrSnO_3 + xA^+ + xe^- \rightarrow A_xSrSnO_3 \quad (5)$$

$$SrSnO_3 + 4A^+ + 4e^- \rightarrow SrO + 2A_2O + Sn \quad (6)$$

$$Sn + xA^+ + xe^- \leftrightarrow A_xSn (0 < x < 4.4) \quad (7)$$

Note that the stoichiometric composition of the intermediate product A_xSrSnO_3 in equation (5) is $A_{2x}Sr_{1-x}SnO_3$, which is consistent with the incorporation mechanism proposed in equation (3). The intrinsic composition of reactants and products of equation (5) is typical for an intercalation anode, where alkali ions occupy interstitial sites during its diffusion through the anode lattice structure [46,47]. This means that both equations (3) and (5) have equivalent significance with respect to defect formation and migration in combining with the discharge process. In the case of $A^+ = Li^+$, the commonly reported conversion and alloying/dealloying processes for SSO anode are well described by equations (6) and (7), respectively [7,8]. Reaction (6) implies the formation of the Sn-metal and inactive SrO [7,8]. During the first discharge, 8.4 Li-ions are stored per unit cell in the SSO anode [7,8].

Two key factors frequently used to explore the capability of a compound as an anode include the open cell voltage (V) and the theoretical capacity (Q) [15,17]. On the one hand, the open cell voltage determines the electrochemical window of the battery, and a low value of V is desirable for the anode. On the other hand, the theoretical capacity (Q) deals with the amount of alkali ion stored by the anode during the charge/discharge process [17]. In neglecting the entropic and pressure effects, the V value can be obtained through the total energy computations by equation (8) [15,17]:

$$V = [E(SrSnO_3) - E(A_xSrSnO_3) - xE(A)] / xF \quad (8)$$

where $E(A_xSrSnO_3)$, $E(SrSnO_3)$ and $E(A)$ represent the total energies of lithiated $SrSnO_3$ with a specific A^+-concentration (x), pristine $SrSnO_3$ and A^+-metal, respectively, and $F = 9.65 \times 10^4$ C mol^{-1} being the Faraday's constant [15,17]. The theoretical capacity can also be determined form the Faraday's Law described by equation (9):

$$Q = zFn/3.6M \quad (9)$$

where the constant of 3.6 is a conversion factor, n and z represent the number of alkali-ions and the valence charge of the alkali ion considered, respectively, and M the molar mass of SSO as an anode [17,27]. Taking the fact that the maximum amount of Li-ion in SSO is known [from Eq. (6)] during discharge into account, without considering the Sn/Li allowing reaction, we assume the same n maximum value for both Na- and K-ions to be stored by SSO.

A supercell of $2 \times 1 \times 1 = 2$-unit cells of SSO is now considered to probe the open cell voltage and the theoretical capacity of the alkalinated SSO, with $n = \{2, 4, 6, 8\}$. Total energy computations of these A-SSO and pristine phases, including the A^+-metal are conducted using the force-field approach. Previous studies [47] used potential-based computations for prediction of V instead of the common DFT approach, taking the advantages of force-field methods to simulate larger systems, and that the force-field parametrization is commonly based on reproduction of the main properties obtained from DFT computations. For the voltage and theoretical capacity computations, equation (3) is also

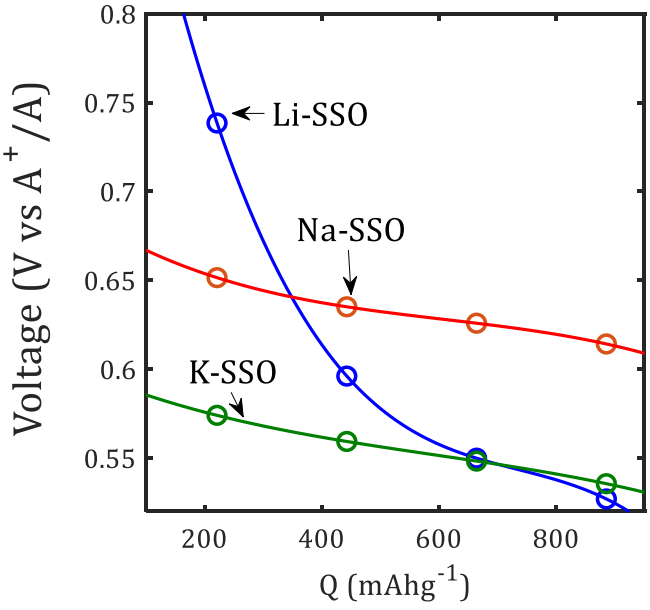

Fig. 4. Discharge voltage/capacity profile of A^+ doped $SrSnO_3$ (A = Li^+, Na^+, K^+). A-SSO denotes Li-, Na- and K-doped $SrSnO_3$.

considered to maintain the neutrality.

Fig. 4 shows the evolution of the open cell voltage with respect to the theoretical capacity computed from equations (8) and (9). Spline interpolation lines are included to idealize the tendencies of the data. Fig. 5 represents the typical voltage/capacity curve for the first cycle [7,8,47,48]. In our model, using the data computed after the initial discharging process, the common slope and plateau profiles usually appear. During the discharge evolution, the Li-SSO shows the highest voltage variation ($\Delta V = 0.21$ V) as compared to the Na- and K-SSO samples ($\Delta V = 0.02$ V). The plateau region for Na-SSO appears at ~0.63 V whereas those for Li- and K- ions emerge at ~0.54 V. In all cases, compounds having the lower voltage values are preferable for an anode in alkali-ion batteries [46,48]. Despite an expected underestimation of DFT and force-field methods in the prediction of the open cell voltage [47,49], the discharge curves follow the common experimental behavior previously reported for Li-SSO sample and other anode compounds [17,46,48].

The morphology and particle-size (micro or nano-size) are factors of significance for the capacity and the long-term Li-cycling stability. For instance, SSO nanorods show a better cycling performance and a higher reversible capacity value than that of its nanoparticle counterpart [8]. The first discharge capacity of SSO nanorods reaches a value of 1400 $mAhg^{-1}$ which is clearly higher than the theoretical value, due to the nanorod structure [7]. Analogously for the SnO_2 anode, the particle size and morphology determine the capacity and cycling of the anode [45,46]. As in nanosized samples, in view of the large surface area and short alkali-diffusion path (due to the presence of unoccupied crystallographic sites, grain boundary or other kind of defects), the intermediate reaction (5) together with equations (6) and (7) can be used to explain the higher capacity of SSO nanorods, by estimation of the amount of alkali ions stored in the sample according to the Faraday's Law.

The main reason to impede a commercialization of Sn-based anodes is their capacity loss during the first cycles attributed to the large volume changes through the discharge process [45,46]. Indeed, a volume change obstructs the formation of the solid electrolyte interface which is decisive for the stability and durability of the battery in preventing further electrolyte decomposition. As the ionic radius of Na^+ and K^+ (larger than the ionic size of Li^+) tends to intensify the volume change, our results concerning the voltage vs theoretical capacity profile of A-SSO are mainly referred to the first discharge cycle. It is not possible to predict the voltage-capacity behavior in the following cycles.

Another key factor determining the anode performance is the alkali diffusion through the anode [13]. A fast alkali ion diffusion ensures a good cyclability in the battery [13]. Diffusion properties are evaluated by the protocol described in Section 2. Fig. 5 displays the temporal evolution of MSD for A^+-ion in nanocrystalline SSO at different temperatures. Upon temperature change, a monotonic increase of the MSD is observed as shown by the slope. Accordingly, a favorable alkali migration through the crystal structure of SSO is actually occurred. In comparison to the Li-diffusion, both Na- and K-migrations are moderately lower, which can be attributable to their larger ionic radius and heavier molar mass.

Diffusion coefficients are computed by fitting with equation (1) using the most linear segments of the MSDs plots. Fig. 6 shows the linearized Arrhenius-type dependency of diffusion coefficient with respect to the inversed temperature. After fitting the diffusion data by equation (2), the activation energies E_a values of 0.25, 0.28 and 0.44 eV are calculated for the Li-, Na- and K-SSO samples, respectively. In addition, the diffusion coefficient at 298 K (D_0) amounts to 9.6×10^{-11}, 2.9×10^{-11} and 4.8×10^{-13} cm^2s^{-1} for Li^+, Na^+ and K^+-doped samples, respectively. As expected, the transport properties are markedly improved following a change of the alkali ionic radius. In this sense, Li^+-doped samples present better large-scale diffusion properties with the lowest activation energy and highest diffusion coefficient at operative temperature, and this followed by Na^+-and K^+-doped samples. It can be noted that SSO can effectively store the Li^+ and Na^+ ion interstitially, resulting in improved transport properties. As a K-SSO sample tends to worsen transport properties, a much more sluggish solid-state diffusion with direct implication on the anode rate capability is probable.

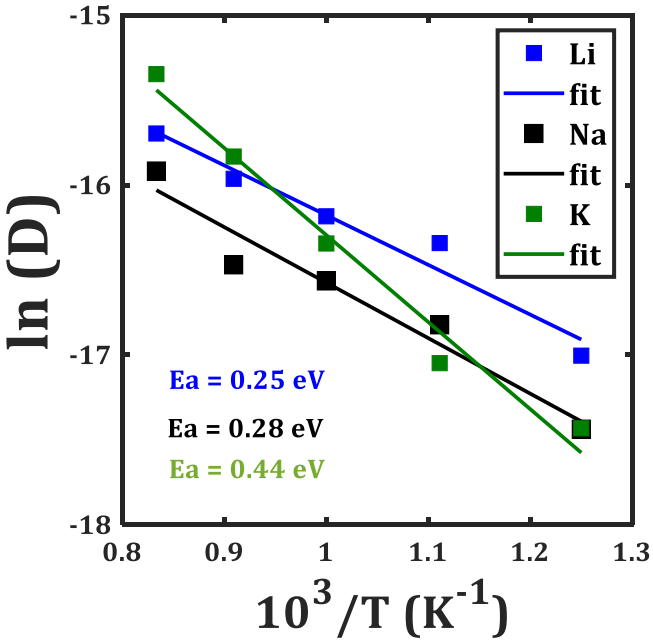

Fig. 6. Arrhenius dependence of A^+- diffusivity (D) for A^+- doped $SrSnO_3$ samples.

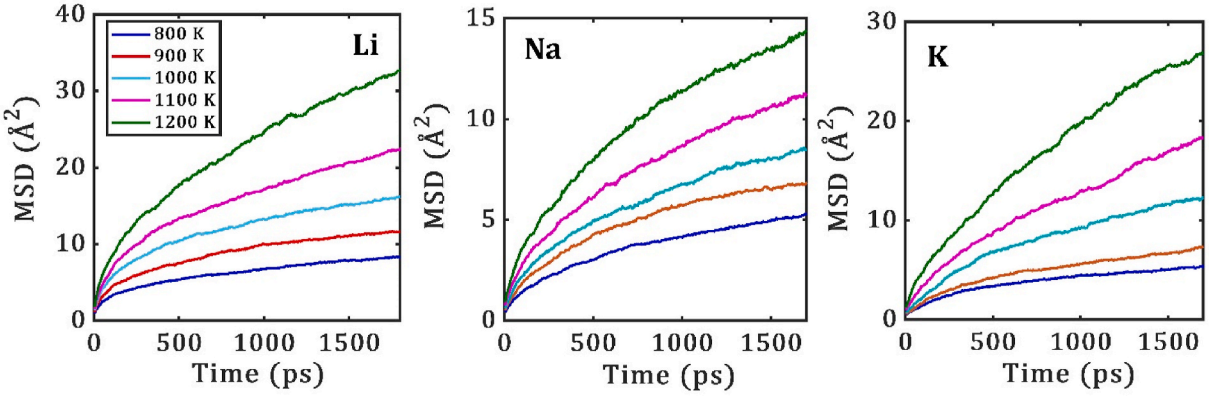

Fig. 5. Alkali-mean square displacements (MSD) versus simulation time at each temperature in nanocrystalline A-SSO samples.

The computed values of D_0 are similar to those of common materials used as electrode in alkali batteries [50–54]. For instance, a similar Li-interstitial mechanism was proven in Li_2SnO_3, resulting in a diffusivity ranging between 6.6 × 10^{-11}-8.7 × 10^{-10} cm^2s^{-1} at operative temperature [16]. Li_2TiO_3 has a diffusion coefficient of 2.1 × 10^{-11} cm^2 s^{-1} at 25 °C [51]. Reported values of Na -ion diffusivity are in the range between 10^{-11}-10^{-12} cm^2 s^{-1} with typical activation energy of 0.3–0.5 eV for $NaVOPO_4$ polymorphs [52]. A comparative study of graphite used as anode for Li- and K-ion batteries pointed out the diffusion coefficients lying in the range of 10^{-11} and 10^{-13} cm^2 s^{-1} at room temperature, respectively [53,54]. Our calculated values for $SrSnO_3$ thus range within the same order of magnitude.

To our knowledge, no previous study is available dealing with the diffusion coefficient and activation energy of Na^+ or K^+ in SSO. Our present predictions reveal an intrinsic mechanism of alkali-insertion into the SSO material during the cycling when it is used as anode in alkali-ion batteries. An intermediate reaction added to complete the description of the first discharge is proposed by the first time, which is necessary for elucidation of the alkali diffusion in SSO lattice structure. Owing to the low diffusion barrier, low open cell voltage, and high capacity, the SSO compound emerges as a potential candidate for negative electrode in the Na-ion batteries. Predictions for the alternative K-ion batteries are less promising.

4. Concluding remarks

In the present theoretical study, various levels of atomistic simulations were performed to predict the potentiality of $SrSnO_3$ as an anode in alkali metal ion batteries. Results of the ground state properties reveal that a doping of the cation Li^+, Na^+ and K^+ into the $SrSnO_3$ lattice structure induces the apparition of extra energy levels in both valence and conduction bands. Energy gaps decrease with respect to the alkali ionic radius, and values are slightly smaller in comparison to the pristine sample. In particular, the K^+-doped $SrSnO_3$ sample is characterized by the smallest energy gap of 2.3 eV.

Defect energetic computations confirmed the strong $A_i^{\bullet}$ -V''_{Sr} - $A_i^{\bullet}$ cluster formation and low energetic cost of the alkali incorporation mechanism proposed in this work. The defect energetic behavior also depends on the alkali ionic radius, in which the smaller Li^+ and Na^+ cations can more easily be introduced into the $SrSnO_3$ lattice structure with a low energetic cost, whereas the larger K^+ ion can also occupy interstitial sites but with a higher energy penalty.

Large-scale molecular dynamic simulations were further used to explore the capability of $SrSnO_3$ using as an alkali ion battery material. For this purpose, transport properties of polycrystalline samples of A^+-doped $SrSnO_3$ were studied. Our calculated results reveal that the diffusion activation energy is lower in Li^+ - (Ea = 0.25 eV) with a higher diffusion coefficient at operative temperature, followed by Na^+- and K^+-doped $SrSnO_3$. Overall, the present study provides us with an intrinsic mechanism of alkali insertion into $SrSnO_3$ during the cycling when it is used in alkali ion batteries, and a prediction for a new anode for Na- and K-ion batteries.

Author contributions

The manuscript was written through the contributions of all authors. All authors have given approval to the final version of the manuscript.

Declaration of competing interest

The authors declare that they have no known competing financial interests or personal relationships that could have appeared to influence the work reported in this paper.

Acknowledgements

We acknowledge the support for computer time and facilities from Ho Chi Minh City University of Technology (HCMUT), Vietnam National University Ho Chi Minh City (VNU-HCM) for this study. We sincerely thank Dr. Son D. N. Luu at Duy Tan University Vietnam, and Dr. James A. Dawson at Newcastle University UK, for valuable discussion in the preparation of the manuscript.

References

[1] H.R. Liu, J.H. Yang, H.J. Xiang, X.G. Gong, S.H. Wei, Origin of the superior conductivity of perovskite Ba(Sr)SnO_3, Appl. Phys. Lett. 102 (2013) 112109.
[2] M.A.K.Y. Shah, B. Zhu, S. Rauf, N. Mushtaq, M. Yousaf, N. Ali, Z. Tayyab, N. Akbar, C.P. Yang, B. Wang, Electrochemical properties of a Co-doped $SrSnO_{3-\delta}$- based semiconductor as an electrolyte for solid oxide fuel cells, ACS Appl. Energy Mater. 3 (2020) 6323–6333.
[3] K. Ueda, Y. Shimizu, Fabrication of Tb–Mg co-doped $CaSnO_3$ perovskite thin films and electroluminescence devices, Thin Solid Films 518 (2010) 3063–3066.
[4] S. Upadhyay, O. Parkash, D. Kumar, Dielectric relaxation and variable-range-hopping conduction in $BaSn_{1-x}Cr_xO_3$ system, J. Electroceram. 18 (2007) 45–55.
[5] B. Muthukutty, R. Karthik, S.M. Chen, M. Abinaya, Designing novel perovskite-type strontium stannate ($SrSnO_3$) and its potential as an electrode material for the enhanced sensing of anti-inflammatory drug mesalamine in biological samples, New J. Chem. 43 (2019) 12264–12274.
[6] Q. Gao, K. Li, L. Zhao, K. Zhang, H. Li, J. Zhang, Q. Liu, Wide-range band-gap tuning and high electrical conductivity in La- and Pb-doped $SrSnO_3$ epitaxial films, ACS Appl. Mater. Interfaces 11 (2019) 25605–25612.
[7] L. Chao, Y. Zhu, S. Fang, H. Wang, Y. Gui, L. Bi, R. Chen, Preparation and characterization of $SrSnO_3$ nanorods, J. Phys. Chem. Solid. 72 (2011) 869–874.
[8] X. Hu, Y. Tang, T. Xiao, J. Jiang, Z. Jia, D. Li, B. Li, L. Luo, Rapid synthesis of single-crystalline $SrSn(OH)_6$ nanowires and the performance of $SrSnO_3$ nanorods used as anode materials for Li-ion battery, J. Phys. Chem. C 114 (2010) 947–952.
[9] M. Wei, A.V. Sanchela, B. Feng, Y. Ikuhara, H.J. Cho, H. Ohta, High electrical conducting deep-ultraviolet-transparent oxide semiconductor La-doped $SrSnO_3$ exceeding ~3000 scm^{-1}, Appl. Phys. Lett. 116 (2020), 022103.
[10] Y. Zhang, M.P.K. Sahoo, J. Wang, Tuning the band gap and polarization of $BaSnO_3$/$SrSnO_3$ superlattices for photovoltaic applications, Phys. Chem. Chem. Phys. 19 (2017) 7032–7039.
[11] B.J. Kennedy, I. Qasim, K.S. Knight, Low temperature structural studies of $SrSnO_3$, J. Phys. Condens. Matter 27 (2015) 365401.
[12] Y. Kumar, R. Kumar, R.J. Choudhary, A. Thakur, A.P. Singh, Reduction in the tilting of oxygen octahedron and its effects on bandgap with La doping in $SrSnO_3$, Ceram. Int. 46 (2020) 17569–17576.
[13] M.S. Whittingham, Lithium batteries and cathode materials, Chem. Rev. 104 (2004) 4271–4301.
[14] L. Chantelle, A.L. Menezes De Oliveira, B.J. Kennedy, J. Maul, M.R.S. Da Silva, T. M. Duarte, A.R. Albuquerque, J.R. Sambrano, R. Landers, M. Siu-Li, E. Longo, I.M. G. Dos Santos, Probing the site-selective doping in $SrSnO_3$: Eu oxides and its impact on the crystal and electronic structures using synchrotron radiation and DFT simulations, Inorg. Chem. 59 (11) (2020) 7666–7680.
[15] Y.A. Zulueta, P. Geerlings, F. Tielens, M.T. Nguyen, Influence of oxygen-sulfur exchange on the structural, electronic, and stability properties of alkali hexastannates, J. Phys. Chem. C 123 (2019) 24375–24382.
[16] Y.A. Zulueta, M.T. Nguyen, J.A. Dawson, Boosting Li-ion transport in transition-metal-doped Li_2SnO_3, Inorg. Chem. 59 (2020) 11841–11846.
[17] Q. He, B. Yu, Z. Li, Y. Zhao, Density functional theory for battery materials, Energy Environ. Mater. 2 (2019) 264–279.
[18] S.M. de Freitas, G.J.B. Júnior, R.D.S. Santos, M.V. do S. Rezende, Defects and dopant properties of $SrSnO_3$ compound: a computational study, Comput. Condens. Matter. 21 (2019), e00411.
[19] S.M. de Freitas, P.C.L. dos Santos, M.V. do S. Rezende, Investigation of dopant incorporation at $SrSnO_3$ compound, J. Solid State Chem. 279 (2019) 120928.
[20] D.C. Rapaport, The Art of Molecular Dynamics Simulation, second ed., Cambridge University Press, New York: United States of America, 2004.
[21] D. Frenkel, B. Smit, Understanding Molecular Simulation: from Algorithms to Applications, Academic Press, San Diego, 1996.
[22] J. Shi, Z. Wang, Y.Q. Fu, Density functional theory study of diffusion of lithium in Li – Sn alloys, J. Mater. Sci. 51 (2016) 3271–3276.
[23] E. Moreira, J.M. Henriques, D.L. Azevedo, E.W.S. Caetano, V.N. Freire, E. L. Albuquerque, Structural, optoelectronic, infrared and Raman spectra of orthorhombic $SrSnO_3$ from DFT calculations, J. Solid State Chem. 184 (2011) 921–928.
[24] M.A. Sattar, M. Benkraouda, N. Amrane, First-principles investigation on the structural, electronic, vibrational and magnetic properties of the Co-substituted orthorhombic $SrSnO_3$, Physica B 590 (2020) 412216.
[25] T. Alammar, I. Hamm, V. Grasmik, M. Wark, A. Mudring, Microwave-assisted synthesis of perovskite $SrSnO_3$ nanocrystals in ionic liquids for photocatalytic applications, Inorg. Chem. 56 (2017) 6920–6932.
[26] M.A. Green, K. Prassides, P. Day, D.A. Neumann, Structure of the n = 2 and n= ∞ member of the Ruddlesden-Popper series, $Sr_{n+1}Sn_nO_{3n+1}$, Int. J. Inorg. Mater. 2 (2000) 35–41.

[27] Y.A. Zulueta, R. Mut, S. Kaya, J.A. Dawson, M.T. Nguyen, Strontium stannate as an alternative anode material for Li-ion batteries, J. Phys. Chem. C 125 (27) (2021) 14947–14956.
[28] S. Mukherjee, L. Kavalsky, C.V. Singh, Ultrahigh storage and fast diffusion of Na and K in blue phosphorene anodes, ACS Appl. Mater. Interfaces 10 (10) (2018) 8630–8639.
[29] Eftekhari, Z.L. Jian, X.L. Ji, Potassium secondary batteries, ACS Appl. Mater. Interfaces 9 (2017) 4404–4419.
[30] H. Mou, W. Xiao, C. Miao, R. Li, L. Yu, Tin and tin compound materials as anodes in lithium-ion and sodium-ion batteries: a review, Front. Chem. 8 (2020) 1–14.
[31] M. Sha, L. Liu, H. Zhao, Y. Lei, Anode materials for potassium-ion batteries: current status and prospects, Carbon Energy 2 (2020) 350–369.
[32] J. Zheng, Y. Wu, Y. Sun, J. Rong, H. Li, L. Niu, Advanced anode materials of potassium ion batteries: from zero dimension to three dimensions, Nano-Micro Lett. 13 (1) (2021) 1–39.
[33] S.M. Zheng, Y.R. Tian, Y.X. Liu, S. Wang, C.Q. Hu, B. Wang, K.M. Wang, Alloy anodes for sodium-ion batteries, Rare Met. 40 (2) (2021) 272–289.
[34] M.C. Payne, M.P. Teter, D.C. Allan, T.A. Arias, J.D. Joannopoulos, Iterative minimization techniques for ab initio total-energy calculations: molecular dynamics and conjugate gradients, Rev. Mod. Phys. 64 (1992) 1045–1097.
[35] J.P. Perdew, K. Burke, M. Ernzerhof, Generalized gradient approximation made simple, Phys. Rev. Lett. 77 (1996) 3865–3868.
[36] B. Hammer, L.B. Hansen, J.K. Norskov, Improved adsorption energetics within density-functional theory using revised perdew-burke-ernzerhof functionals, Phys. Rev. B Condens. Matter 59 (1999) 7413–7421.
[37] H.J. Monkhorst, J.D. Pack, Special points for brillouin-zone integrations, Phys. Rev. B 13 (1976) 5188.
[38] J.D. Gale, U.L.P. G, A computer Program for the symmetry-adapted simulation of solids, J. Chem. Soc. Faraday Trans. 93 (1997) 629–637.
[39] B.G. Dick, A.W. Overhauser, Theory of the dielectric constants of alkali halide crystals, Phys. Rev. 112 (1958) 90–103.
[40] S. Plimpton, Fast parallel algorithms for short-range molecular dynamics, J. Comput. Phys. 117 (1995) 1–19.
[41] P. Hirel, Atomsk: a tool for manipulating and converting atomic data files, Comput. Phys. Commun. 197 (2015) 212–219.
[42] N.F. Mott, M.J. Littleton, Conduction in polar crystals. I. Electrolytic conduction in solid salt, Trans. Faraday Soc. 34 (1938) 485–499.
[43] J. R. Dahn Courtney, Electrochemical and in situ X-ray diffraction studies of the reaction of lithium with tin oxide composites, J. Electrochem. Soc. 144 (6) (1997) 2045–2052.
[44] Y. Cheng, A. Nie, L.Y. Gan, Q. Zhang, U.A. Schwingenschlögl, Global view of the phase transitions of SnO_2 in rechargeable batteries based on results of high throughput calculations, J. Mater. Chem. A. 3 (38) (2015) 19483–19489.
[45] Nie, L.-Y. Gan, Y. Cheng, H. Asayesh-Ardakani, Q. Li, C. Dong, R. Tao, F. Mashayek, H.-T. Wang, U. Schwingenschlögl, R.F. Klie, R.S. Yassar, Atomic-scale observation of lithiation reaction front in nanoscale SnO_2 materials, ACS Nano 7 (7) (2013) 6203–6211.
[46] F. Zoller, D. Böhm, T. Bein, D. Fattakhova-Rohlfing, Tin oxide based nanomaterials and their application as anodes in lithium-ion batteries and beyond, ChemSusChem 12 (2019) 4140–4159.
[47] J.P. Pender, G. Jha, D.H. Youn, J.M. Ziegler, I. Andoni, E.J. Choi, A. Heller, B. S. Dunn, P.S. Weiss, R.M. Penner, C.B. Mullins, Electrode degradation in lithium-ion batteries, ACS Nano 14 (2020) 1243–1295.
[48] M. Islam, A. Ostadhossein, O. Borodin, A.T. Yeates, W.W. Tipton, R.G. Hennig, N. Kumar, A.C.T. Van Duin, ReaxFF molecular dynamics simulations on lithiated sulfur cathode materials, Phys. Chem. Chem. Phys. 17 (2015) 3383–3393.
[49] M.G. Medvedev, I.S. Bushmarinov, J. Sun, J.P. Perdew, K.A. Lyssenko, Density functional theory is straying from the path toward the exact functional, Science 355 (2017) 49–52.
[50] Y.A. Zulueta, M.T. Nguyen, Lithium hexastannate: a potential material for energy storage, Phys. Status Solidi B 255 (2018) 1700669.
[51] K. Mukai, M. Yashima, K. Hibino, T. Terai, Experimental visualization of interstitialcy diffusion of Li ion in β-Li_2TiO_3, ACS Appl. Energy Mater. 2 (2019) 5481–5489.
[52] P.A. Aparicio, J.A. Dawson, M.S. Islam, N.H.D. Leeuw, Computational study of $NaVOPO_4$ polymorphs as cathode materials for Na-ion batteries: diffusion, electronic properties, and cation-doping behavior, J. Phys. Chem. C 122 (2018) 25829–25836.
[53] R.A. Adams, A. Varma, V.G. Pol, Temperature dependent electrochemical performance of graphite anodes for K-ion and Li-ion batteries, J. Power Sources 410–411 (2019) 124–131.
[54] H.V. Ramasamy, B. Senthilkumar, P. Barpanda, Y. Lee, Superior potassium-ion hybrid capacitor based on novel P3-type layered, Chem. Eng. J. 368 (2019) 235–243.